Radio Science, Volume 26, Number 6, Pages 1419–1434, November–December 1991

Error analysis of image reconstruction by a synthetic aperture interferometric radiometer

Christopher S. Ruf

Jet Propulsion Laboratory, California Institute of Technology, Pasadena

(Received April 29, 1991; revised September 3, 1991; accepted September 3, 1991.)

An error analysis is presented for the image reconstruction algorithm currently employed by the electronically steered thinned array radiometer aircraft instrument. This instrument samples components of the Fourier transform of the brightness temperature distribution at 1.4 GHz. Sources of error are identified, including systematic offsets and stochastic noise in the measurements, errors in the interference pattern antenna calibration, multipath scattering from the antenna support structure, mutual coupling between nearby array elements, and variations in the antenna patterns of the array elements. These errors are shown to produce artifacts in the image which appear as "streaks" running along the instrument flight line. Possible hardware corrections are discussed. These include a reduction in the profile of the antenna support structure and a decoupling of adjacent and other nearby array elements using corrugated "skirts." Also discussed are several image enhancement techniques which detect and correct for some of the streaking. These techniques include a renormalization of the interference patterns based on the measured element patterns, a perturbation based interpretation of image contrast, and a covariance analysis of noise present in the image.

1. INTRODUCTION

Projected future requirements for the spatial resolution of microwave radiometers in low and geosynchronous Earth orbit (LEO and GEO) will demand electrically large antenna systems. For example, spatial resolution of 10 km requires a 50 wavelength antenna in LEO at 400 km altitude and a 4500 wavelength antenna in GEO. A satisfactory response to the "Mission to Planet Earth" requirements for the monitoring of key global change parameters will require this resolution at microwave frequencies which are suitable for imaging soil moisture (1.4 GHz, 21-cm wavelength) and ocean salinity (1.4 and 2.65 GHz, 21- and 11-cm wavelength) [*Murphy et al.*, 1987]. These antenna sizes cannot be practically accommodated by conventional mechanically steered reflector designs. One promising alternative is the synthetic aperture interferometric radiometer (SAIR). This approach uses the aperture synthesis process by which radio astronomers have generated very large effective antennas by cross correlating an array of widely spaced antenna elements. An effective aperture is synthesized which is as large as the widest spacing between elements in the sparsely filled array of real antennas. The number of elements needed is significantly reduced below that of a conventional phased array, and the mass and weight are both reduced well below that needed for a conventional reflector antenna with similar performance. In addition, the antenna beam is steered electrically, so that the problems with mechanical steering are also eliminated.

An aircraft prototype has been built based on this concept. It is called the electronically steered thinned array radiometer (ESTAR), operating at 1.4 GHz with a synthesized antenna aperture of 3.5 wavelengths. The system design characteristics are described by *Hiett* [1988], and initial flight images are presented by *Le Vine et al.* [1990]. The initial image reconstruction algorithm used to generate the flight images is developed by *Tanner* [1990]. The work presented here is an analysis of the errors in the brightness temperature image reconstructed by ESTAR from its raw measurements. The analysis is divided into four parts. Section 2 is a review of the fundamental principles of interferometric aperture synthesis, followed by a brief description of the ESTAR hardware and reconstruction algorithm. Section 3 considers the different sources of error in the image. Included here are multipath effects on

Paper number 91RS02355.
0048-6604/91/91RS-02355$08.00

the interference patterns, antenna element pattern envelope effects, and stochastic and systematic noise in the measurements. Section 4 examines the inherent errors associated with the reconstruction of uniform scenes, those without contrast. This error can be partially corrected using an antenna element pattern renormalization and can be calibrated with an image perturbation procedure. Section 5 derives the correlation structure of the errors in the image. An oscillating correlation between the noise in different image pixels is found to result from the multipath interference. This correlation, when coupled with systematic biases in the measurements or in the system calibration, will produce pronounced "streaks" in the image.

2. REVIEW OF SAIR IMAGING

SAIR imaging is based on a fundamental spatial filtering characteristic of interferometer pairs of antennas. The effective antenna pattern formed by two separated antennas whose signals are cross-correlated together contains a sinusoidally varying series of interference maxima and minima, enveloped by the patterns of the two antennas. The frequency of the sinusoidal variation increases as the antenna separation is increased. When used with a microwave radiometer receiver, this effective antenna pattern acts as a spatial filter; it is most sensitive to variations in the scene brightness temperature distribution with the same sinusoidal variation. Coherent quadrature detection in the receiver essentially extracts the sine and cosine components of the spatial Fourier transform of the brightness temperature distribution at a frequency determined by the spacing between the interferometer pair. An image can be formed by adequately sampling the spatial Fourier transform, or visibility space, of the brightness temperature distribution. An equivalent Nyquist sampling criteria exists which stipulates that visibility measurements be made at interferometer pair spacings in increments of approximately one-half wavelength in LEO and 2.8 wavelengths in GEO. This follows from the angular extent of the brightness temperature distributions which are viewed from LEO ($\approx \pm 90°$) and GEO ($\approx \pm 9°$). The maximum spacing in the visibility domain will determine the spatial resolution in the brightness temperature domain in a manner exactly analogous to standard time and frequency sampling/resolution relationships.

A derivation of the Fourier transform relationship between visibility samples and the brightness temperature distribution is given by *Ruf et al.* [1988]. In GEO, with small flood beam antenna elements covering the entire Earth disk, a visibility sample is given by

$$V(u, v) = \int_0^{2\pi} \int_0^{\pi} T_B(\theta, \phi) P(\theta, \phi) \cdot e^{j2\pi(u \sin\theta \cos\phi + v \sin\theta \sin\phi)} \sin\theta \, d\theta \, d\phi \quad (1)$$

where u and v are the relative coordinates of the interferometer pair in the plane of the antenna array in units of wavelengths, $T_B(\theta, \phi)$ is the brightness temperature distribution across the Earth and cold space, and $P(\theta, \phi) = E_1(\theta, \phi) E_2^*(\theta, \phi)$ where $E_{1,2}(\theta, \phi)$ are the electric field radiation patterns of the two antenna elements and the asterisk denotes complex conjugation. The coordinate system relating u, v, θ, and ϕ is described in Figure 1*a*. In LEO, one possible antenna configuration consists of a line of unevenly spaced antenna elements, each element having a long, thin (fan beam) antenna pattern. All of the fan beams overlap, defining a brightness temperature strip on the Earth surface to be imaged. Pixels along the strip can be resolved by interferometry and the strip can be oriented cross track to the direction of motion, so that forward motion will create a "pushbroom" imager. The visibility samples for this type of SAIR are given by [*Ruf et al.*, 1988]:

$$V(n) = \int_{-\pi}^{\pi} T_B(\phi) P(\phi) e^{j\pi n \sin\phi} \, d\phi \quad (2)$$

where n is the number of half wavelengths between the interferometer pair, $T_B(\phi)$ is the brightness temperature distribution along the strip, ϕ is the off-nadir angle along the strip, and $P(\phi) = \int_0^{\pi} E_1(\theta, \phi) \, E_2^* \, (\theta, \phi) \sin\theta \, d\theta$, where $E_{1,2}(\theta, \phi)$ are the electric field radiation patterns of the two antenna elements with the narrow dimension of their fan beams oriented in the θ direction. The coordinate system relating the orientation of the antenna elements to θ and ϕ is described in Figure 1*b*.

Nyquist sampling of the visibility function insures that the image reconstruction does not suffer from aliasing. Here aliasing is equivalent to increased sidelobes in the synthesized antenna pattern. The visibility function can be adequately sampled by an

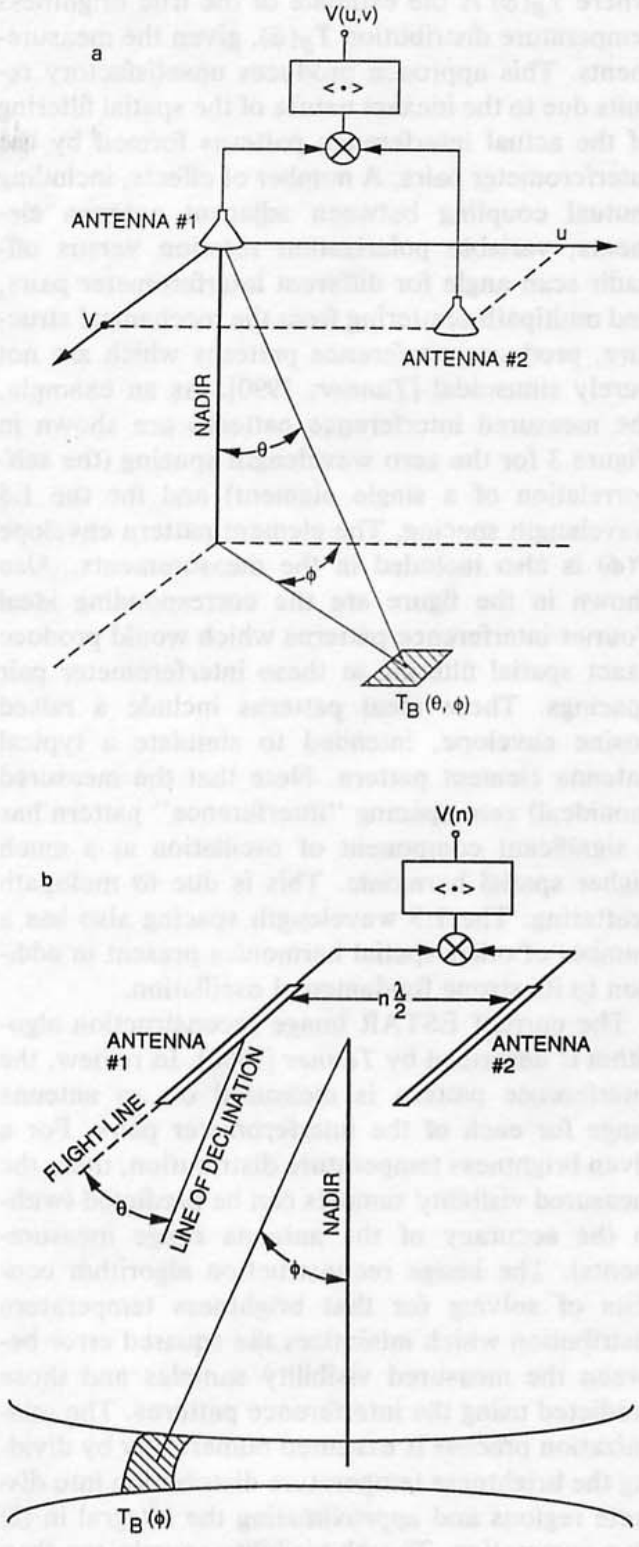

Fig. 1. Coordinate systems and orientation for synthetic aperture interferometric radiometers. (*a*) Two-dimensional synthesis using small, flood beam antenna elements and (*b*) one-dimensional synthesis using long, thin, fan beam antenna elements. The ESTAR instrument uses one-dimensional synthesis.

array of antenna elements which is significantly thinned out, relative to a uniform grid (in two dimensions) or a uniform line (in one dimension) of elements. This thinning procedure has been examined for one-dimensional synthesis in LEO [*Moffett*, 1968; *Ruf et al.*, 1988] and for two-dimensional synthesis in GEO [*Ruf*, 1990]. All necessary spacings between interferometer pairs are sampled by cross correlating all possible pairs of antennas in the thinned array. The fact that this thinning can be so pronounced, and in fact increases, as a percentage of the equivalent uniformly filled array, with increasing antenna size, is largely responsible for the attractiveness of the SAIR approach to synthesis of electrically large antennas in space.

The degree of thinning possible in one dimensional synthesis has been studied as a number theoretic problem [*Leech*, 1956]. Leech found that, in the limit of very large thinned arrays, optimally thinned configurations are bounded by

$$2+\frac{4}{3\pi}\le \lim_{n\to\infty}\frac{k^2}{n}\le\frac{8}{3} \tag{3}$$

where n is the maximum number of unit spacings in the array (typically one-half wavelength) and k is the minimum number of elements. The spatial resolution of the one-dimensional SAIR imager is inversely proportional to its maximum spacing. For a n half-wavelength maximum spacing the resolution is approximately [*Ruf et al.*, 1988]:

$$\text{HPBW}=\frac{2}{n}\ \text{rad} \tag{4}$$

where HPBW is the half power beamwidth of the synthesized antenna pattern. Combining (3) and (4), the minimum number of antenna elements, k, required is bounded by

$$\frac{2.20}{\text{HPBW}^{1/2}}\le k\le\frac{2.31}{\text{HPBW}^{1/2}} \tag{5}$$

Note that the number of elements required only increases as the square root of the resolution. This is in contrast to the linear relationship between antenna element count and array resolution for a uniformly filled linear array antenna. The number of elements (as well as the power, weight, and cost) has been reduced significantly. However, this reduction in real antenna size also reduces the signal

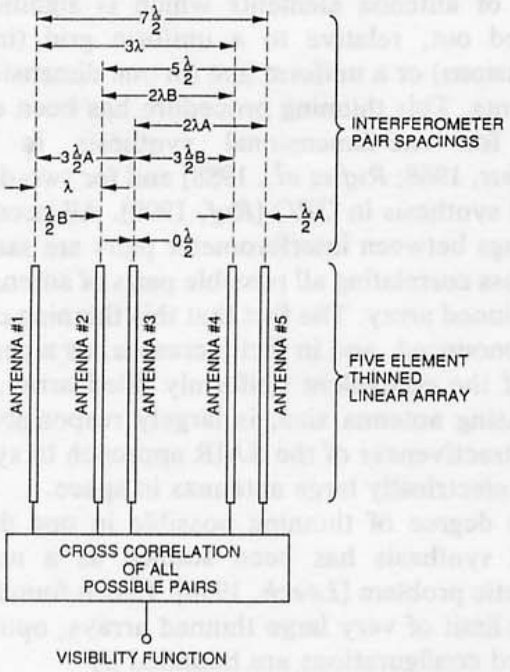

Fig. 2. Antenna array configuration for the ESTAR aircraft instrument. Also shown are all possible interferometer pairs which are formed by cross correlation of the individual antenna outputs. Note that three of the interferometer pairs, those with spacings of 0.5λ, 1.5λ, and 2.0λ, are each formed twice [from *Tanner*, 1990].

to noise ratio of the reconstructed image [*Ruf et al.*, 1988]. This imposes practical limits on the thinning that is possible with very large antennas.

The aircraft prototype ESTAR instrument is a one dimensional synthesis SAIR with five fan beam antenna elements in its array. A schematic of the antenna configuration is shown in Figure 2. Cross correlations of all possible pairs of antenna elements produce samples of the visibility function at interferometer spacings of 0, 1, 2, $\cdots$, 7 half wavelengths. These spacings are labeled in Figure 2. Also, shown in the figure are the redundant spacings, those sampled more than once, which are labeled "A" and "B."

A "naive" attempt to invert (2) and solve for $T_B(\phi)$ would result in an inverse Fourier transform image reconstruction algorithm of the form [*Ruf et al.*, 1988]:

$$\hat{T}_B(\phi) = \frac{1}{P(\phi)} \sum_{n=-N}^{N} V(n) e^{-j\pi n \sin\phi} \tag{6}$$

where $\hat{T}_B(\phi)$ is the estimate of the true brightness temperature distribution $T_B(\phi)$, given the measurements. This approach produces unsatisfactory results due to the inexact nature of the spatial filtering of the actual interference patterns formed by the interferometer pairs. A number of effects, including mutual coupling between adjacent antenna elements, variable polarization rotation versus off-nadir scan angle for different interferometer pairs, and multipath scattering from the mechanical structure, produce interference patterns which are not purely sinusoidal [*Tanner*, 1990]. As an example, the measured interference patterns are shown in Figure 3 for the zero wavelength spacing (the self-correlation of a single element) and for the 1.5 wavelength spacing. The element pattern envelope $P(\phi)$ is also included in the measurements. Also shown in the figure are the corresponding ideal Fourier interference patterns which would produce exact spatial filtering at these interferometer pair spacings. These ideal patterns include a raised cosine envelope, intended to simulate a typical antenna element pattern. Note that the measured (nonideal) zero spacing "interference" pattern has a significant component of oscillation at a much higher spatial harmonic. This is due to multipath scattering. The 1.5 wavelength spacing also has a number of other spatial harmonics present in addition to its strong fundamental oscillation.

The current ESTAR image reconstruction algorithm is described by *Tanner* [1990]. In review, the interference pattern is measured on an antenna range for each of the interferometer pairs. For a given brightness temperature distribution, then, the measured visibility samples can be predicted (within the accuracy of the antenna range measurements). The image reconstruction algorithm consists of solving for that brightness temperature distribution which minimizes the squared error between the measured visibility samples and those predicted using the interference patterns. The minimization process is executed numerically by dividing the brightness temperature distribution into discrete regions and approximating the integral in (2) by a summation. The ith visibility sample can then be described by

$$V_i = \sum_{j=1}^{M} g_{ij} T_j \tag{7}$$

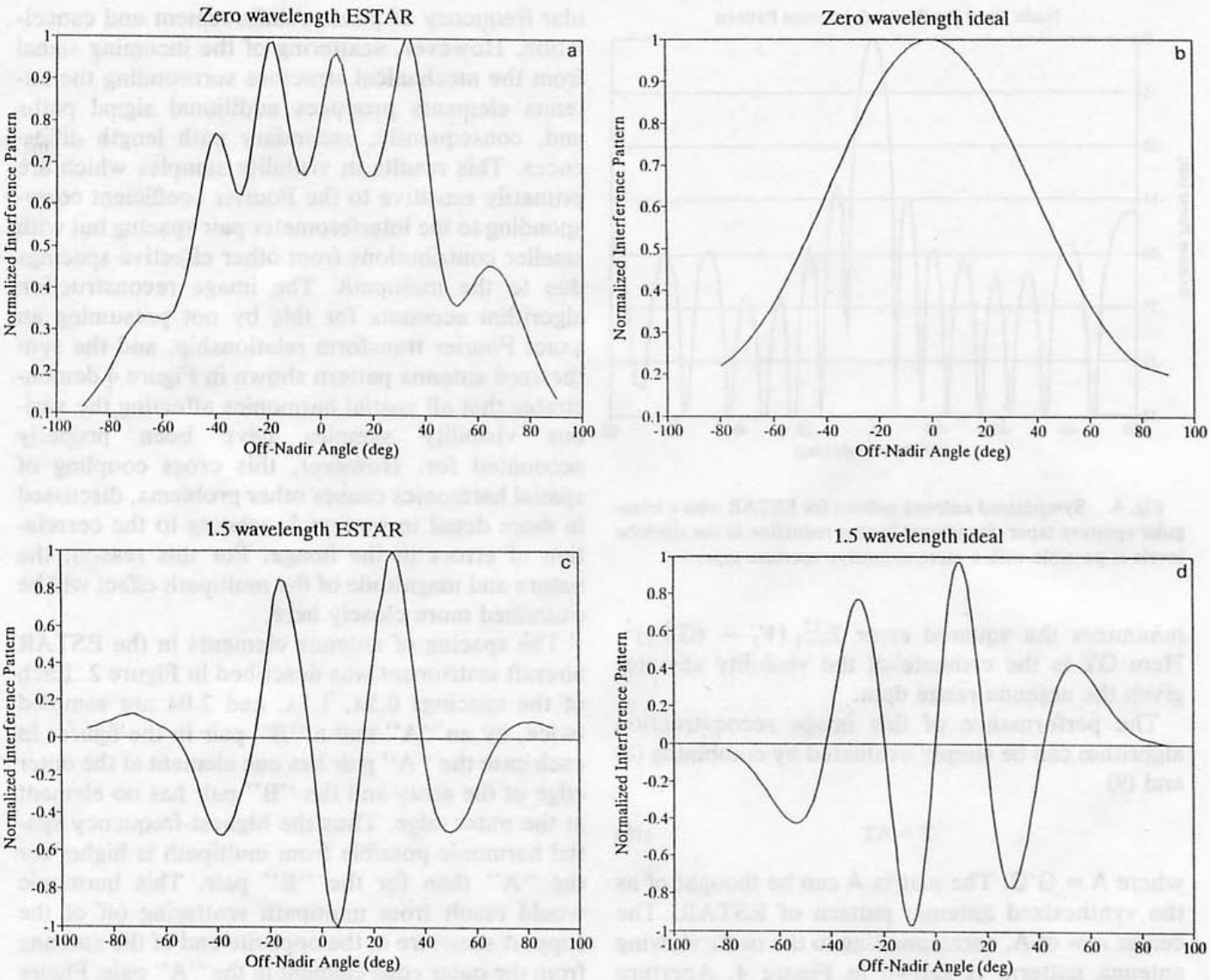

Fig. 3. Measured and theoretical interference patterns for a one-dimensional SAIR array. (*a*) Measured self-correlation of one antenna element in the ESTAR array. Note the presence of higher-frequency oscillations due to multipath scattering. (*b*) Theoretical self-correlation without any multipath effects, including a raised cosine element pattern envelope. (*c*) Measured interference pattern for a 1.5λ interferometer pair spacing. (*d*) Theoretical interference pattern for a 1.5λ spacing, assuming no spatial harmonics other than that due to the 1.5λ spacing are present.

where g_{ij} is the sensitivity of V_i to brightness temperature at the jth pixel in the image, T_j is the brightness at the jth pixel, and M is the total number of pixels in the image.

The complete measurement of visibility samples made for a given brightness temperature distribution can then be represented by

$$\mathbf{V} = \mathsf{G}\mathbf{T} \tag{8}$$

where $\mathbf{V}$ is the vector of measurements, G is the matrix of sensitivities g_{ij}, and $\mathbf{T}$ is a vector representing the brightness temperature distribution lying within the antenna element pattern. Two rows of G were plotted in Figures 3*a* and 3*c*. The image reconstruction algorithm then follows as a generalized matrix inversion of (8)

$$\hat{\mathbf{T}} = \mathsf{G}'\mathbf{V} \tag{9}$$

where $\hat{\mathbf{T}}$ is the estimate of the brightness temperature distribution vector and $\mathsf{G}' = \mathsf{G}^{\dagger}(\mathsf{G}\mathsf{G}^{\dagger})^{-1}$, where the dagger is the matrix transpose operator. This estimator solves for that image, $\hat{\mathbf{T}}$, which

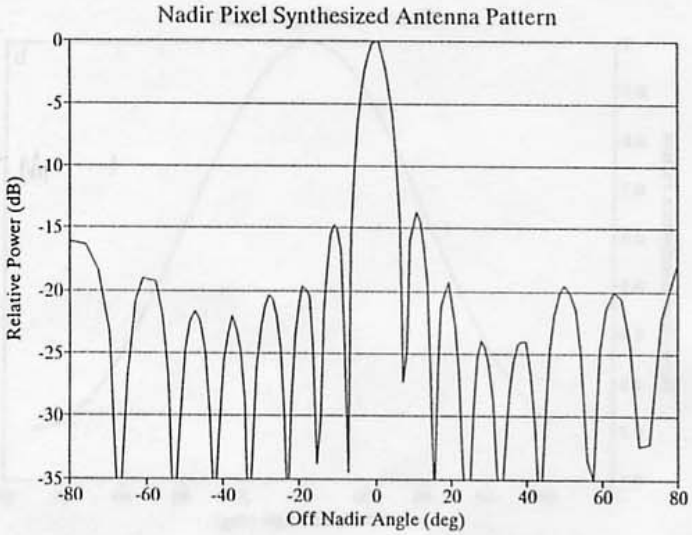

Fig. 4. Synthesized antenna pattern for ESTAR with a triangular aperture taper. Significant further reduction in the sidelobe levels is possible with a more extensive aperture taper.

minimizes the squared error $\Sigma_{i=1}^{15} [V_i - (\mathbf{G}\hat{\mathbf{T}})_i]^2$. Here $\mathbf{G}\hat{\mathbf{T}}$ is the estimate of the visibility samples given the antenna range data.

The performance of this image reconstruction algorithm can be simply evaluated by combining (8) and (9)

$$\hat{\mathbf{T}} = \mathbf{A}\mathbf{T} \tag{10}$$

where $\mathbf{A} = \mathbf{G}'\mathbf{G}$. The matrix $\mathbf{A}$ can be thought of as the synthesized antenna pattern of ESTAR. The center row of $\mathbf{A}$, corresponding to the nadir viewing antenna pattern, is shown in Figure 4. Aperture tapers can be applied, in order to reduce the sidelobes in the pattern, by weighting the visibility samples, in a manner analogous to conventional antenna tapers.

3. SOURCES OF IMAGE RECONSTRUCTION ERROR

Several hardware and measurement related effects produce errors in the brightness temperature images that are reconstructed from the visibility samples. The Fourier transform relationship between visibility samples and the observed brightness temperature distribution results from the interference pattern formed by cross correlating separated antenna elements. This, in turn, results from the difference in path length from the brightness temperature source to the two antennas. A particular path length difference produces a particular frequency of phase reinforcement and cancellation. However, scattering of the incoming signal from the mechanical structure surrounding the antenna elements produces additional signal paths and, consequently, secondary path length differences. This results in visibility samples which are primarily sensitive to the Fourier coefficient corresponding to the interferometer pair spacing but with smaller contributions from other effective spacings due to the multipath. The image reconstruction algorithm accounts for this by not presuming an exact Fourier transform relationship, and the synthesized antenna pattern shown in Figure 4 demonstrates that all spatial harmonics affecting the various visibility samples have been properly accounted for. However, this cross coupling of spatial harmonics causes other problems, discussed in more detail in section 5, relating to the correlation of errors in the image. For this reason, the nature and magnitude of the multipath effect will be examined more closely here.

The spacing of antenna elements in the ESTAR aircraft instrument was described in Figure 2. Each of the spacings 0.5λ, 1.5λ, and 2.0λ are sampled twice, by an "A" and a "B" pair in the figure. In each case the "A" pair has one element at the outer edge of the array and the "B" pair has no element at the outer edge. Thus the highest-frequency spatial harmonic possible from multipath is higher for the "A" than for the "B" pair. This harmonic would result from multipath scattering off of the support structure at the opposite end of the antenna from the outer edge element in the "A" pair. Figure 5 shows the power spectrum of the interference pattern of each of these redundant interferometer spacings. For each spacing the "A" pair is shown as a solid line and the "B" pair as a dashed line. All of these spectra peak at the spatial harmonic appropriate for their interferometer pair spacing. However, the "A" pairs all have a weak secondary peak at a spatial harmonic corresponding to a spacing of four wavelengths. This is the multipath effect. The "B" pairs have a multipath harmonic contribution which, in each case, corresponds to the greatest separation between its elements and the antenna support structure. These higher-frequency spatial harmonics stand out clearly in the figure because they are well separated from the fundamental harmonic contribution. However, these is also much additional harmonic contribution from spatial frequencies near the fundamental, due to additional

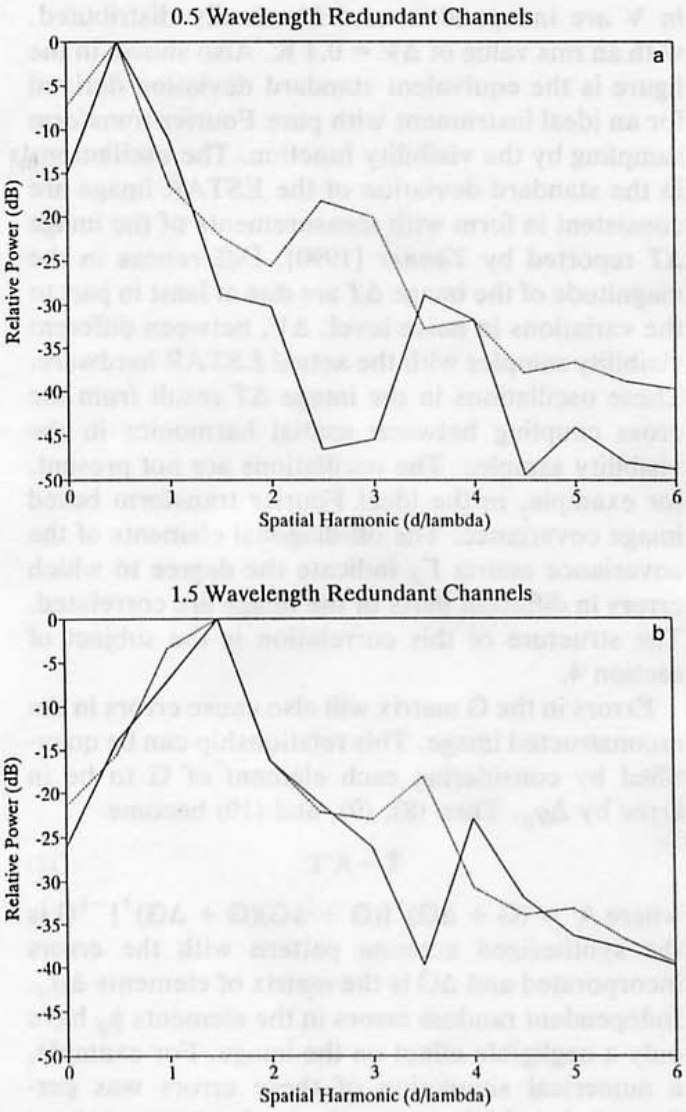

Fig. 5. Power spectrum of the ESTAR interference patterns of the redundant interferometer pairs. In each case the solid line represents the pair with one element at the outer edge of the antenna array. The dashed line represents the pair with neither element at the outer edge. Note the secondary peak near 4λ for each solid line, due to multipath interference with the opposite far edge of the antenna support structure. (*a*) 0.5λ spacing; (*b*) 1.5λ spacing; (*c*) 2.0λ spacing.

multipath between the elements and closer edges of the antenna support structure. In fact, the figure indicates a strong inverse correlation between the power in a particular harmonic due to multipath and the distance between the element and the edge structure with which it is interfering to generate that harmonic. The effect of this cross coupling between harmonics on image reconstruction errors will be examined in section 5.

The "interference" pattern for the zeroth visibility sample was shown in Figure 3*a*. To the extent that the Fourier transform relationship between brightness temperature distribution and visibility function is valid, this sample represents the bias, or "D.C. offset," of the distribution, about which zero mean perturbations make up the contrast in the image. It is a brightness temperature pedestal on which cross track variations in the scene sit. For many Earth remote sensing applications this is a very useful perspective because nonlinear geophysical retrieval algorithms are often devised as first order perturbations about a nominal geophysical condition. The brightness temperature pedestal provides a natural baseline about which to expand the perturbation. This approach also avoids the problems with errors in the reconstruction of the actual nominal brightness temperature distribution. Actual brightness temperature distributions will rarely, if ever, appear similar to the "interference" pattern of the zeroth visibility sample. Thus the true brightness temperature distribution will be poorly reconstructed. However, perturbations about a nominal distribution are well represented by a linear combination of the higher-order spatial harmonics. This approach is described in more detail in section 4.

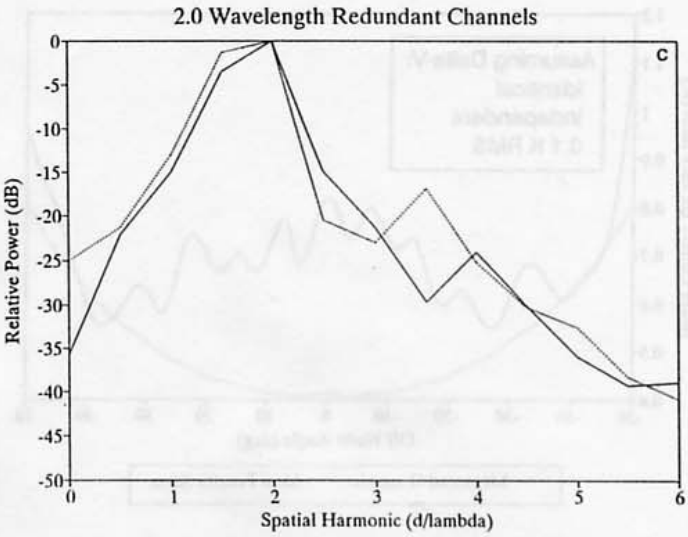

Fig. 5. (continued)

The image reconstruction algorithm described by (9) has two sources of error. Measurement errors are accounted for by uncertainties, ΔV, in the measured visibility function. The interference patterns assumed for each interferometer pair may also be in error. This corresponds to uncertainties, Δg_{ij}, in the elements of the G matrix. The ΔV uncertainty

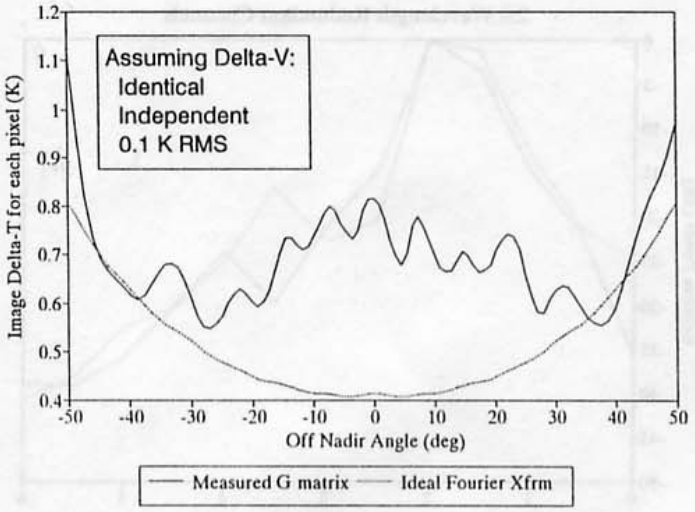

Fig. 6. Theoretical additive rms noise ΔT in the image due to an assumed additive rms noise level in the visibility samples, ΔV, of 0.1 K. The solid line assumes the ESTAR interference patterns. The dashed line assumes ideal Fourier transform interference patterns.

can result from both systematic offsets in the data, due to inaccurate calibration, and random, zero mean, measurement noise. The random component of ΔV is analogous to the measurement uncertainty ΔT present in all conventional microwave radiometers. The systematic biases in the visibility samples are harder to predict since they typically result from an incomplete or incorrect accounting for the sources of offsets and gain corrections made when calibrating an instrument. Uncertainties in elements of the G matrix can result from measurement errors during the antenna range determination of the interference patterns and from changes in the patterns themselves between the antenna range tests and the subsequent aircraft flights. Changes of the latter type might result, for example, from differences in the near-field mechanical environment surrounding the antenna array.

The effects of uncertainties in the visibility function on the reconstructed image can be factored directly from (9)

$$\Gamma_T = (\mathsf{G}')\Gamma_v(\mathsf{G}'^{\dagger}) \tag{11}$$

where Γ_T is the covariance on $\hat{\mathbf{T}}$ and Γ_v is the covariance on $\mathbf{V}$. The main diagonal of Γ_T represents the variance on each pixel in the brightness temperature reconstruction. The square root of this variance is shown in Figure 6 as a function of off-nadir angle. This figure assumes that the errors in $\mathbf{V}$ are independent and identically distributed, with an rms value of $\Delta V = 0.1$ K. Also shown in the figure is the equivalent standard deviation derived for an ideal instrument with pure Fourier transform sampling by the visibility function. The oscillations in the standard deviation of the ESTAR image are consistent in form with measurements of the image ΔT reported by *Tanner* [1990]. Differences in the magnitude of the image ΔT are due at least in part to the variations in noise level, ΔV, between different visibility samples with the actual ESTAR hardware. These oscillations in the image ΔT result from the cross coupling between spatial harmonics in the visibility samples. The oscillations are not present, for example, in the ideal Fourier transform based image covariance. The off-diagonal elements of the covariance matrix Γ_T indicate the degree to which errors in different parts of the image are correlated. The structure of this correlation is the subject of section 4.

Errors in the G matrix will also cause errors in the reconstructed image. This relationship can be quantified by considering each element of G to be in error by Δg_{ij}. Then (8), (9), and (10) become

$$\hat{\mathbf{T}} = \mathsf{A}'\mathbf{T} \tag{12}$$

where $\mathsf{A}' = (\mathsf{G} + \Delta\mathsf{G})^{\dagger}[(\mathsf{G} + \Delta\mathsf{G})(\mathsf{G} + \Delta\mathsf{G})^{\dagger}]^{-1}\mathsf{G}$ is the synthesized antenna pattern with the errors incorporated and $\Delta\mathsf{G}$ is the matrix of elements Δg_{ij}. Independent random errors in the elements g_{ij} have only a negligible effect on the image. For example, a numerical simulation of these errors was performed, in which the synthesized antenna pattern A′ was computed for different levels of error in G. The antenna gain, averaged over the main beam, was determined for each of 100 realizations at each error level. The results are shown in Figure 7. The gain of the synthesized antenna pattern decreased by only 1% with a 5% random error in the G matrix. This decrease in gain can be equated approximately with a corresponding increase by 1% in the integrated sidelobe level (or decrease by 1% in the beam efficiency). This small impact on the image results because many of the G matrix elements are linearly dependent. This oversampling averages down the individual errors in the matrix elements.

Systematic errors in the G matrix are not reduced by averaging, and they will have a more significant impact on errors in the image. The most likely sources of systematic errors are inaccurate gain and offset corrections in the individual cross-correlator

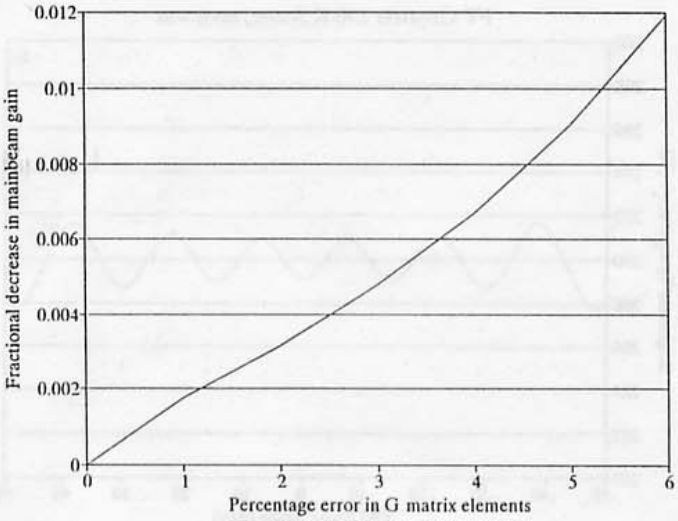

Fig. 7. Decrease in the average gain of the synthesized antenna pattern over the main beam due to independent errors in the individual measurements of the interference patterns. The antenna pattern is largely unaffected because the interference patterns have been greatly oversampled.

channels of ESTAR. These errors can equivalently be modeled as uncertainties in the visibility samples themselves, since they will affect all columns of a particular row of G equally. The covariance formalism developed above for the visibility function errors can also account for these systematics.

4. UNIFORM SCENE ERRORS AND IMAGE RECOVERY

The idealized relationship between visibility function and brightness temperature distribution described in (2) presumes two important simplifications. One, the uncoupled filtering of Fourier components by each visibility sample, has been discussed above. The other is the identification of a unique antenna element pattern $P(\phi)$ for the entire array of interferometer pairs. In fact, the element patterns which envelope each interference pattern are slightly different, due to near-field effects in the antenna structure and to small differences in the individual antenna elements. Thus image reconstruction cannot solve for a unique function, $T_B(\phi)P(\phi)$, which can then be solved for $T_B(\phi)$. Instead, the reconstruction algorithm attempts to solve directly for $T_B(\phi)$ by measuring the complete element-pattern-weighted interference patterns and inverting the integral equation with respect to $T_B(\phi)$. This procedure produces a "best" image, in a minimum squared error sense, which is poorly suited to the reconstruction of uniform brightness temperature scenes. This section examines the extent of the reconstruction error for a uniform scene and suggests two possible refinements to the image reconstruction algorithm to reduce the error.

The set of interference patterns for all interferometer pairs in ESTAR forms a basis over a subspace of all possible brightness temperature distributions. All distributions in that subspace can be constructed by linear combinations of the interference patterns. Only distributions in the subspace can be reconstructed exactly by ESTAR, and those lying outside the subspace are approximated by the nearest element in the subspace (nearest in the sense of minimum squared error). Thus uniform brightness temperature distributions, as well as very slowly varying scenes such as the open ocean, can only be approximated. The degree of approximation is shown in Figure 8. A uniform 290 K scene has been reconstructed, using both the measured interference patterns and the ideal, Fourier transform, patterns. (The zero and 1.5 wavelength spacing ideal patterns were shown in Figure 3.) These images both include a triangular aperture taper to reduce the synthesized antenna pattern's sidelobe levels. Note that, in both cases, a significant amount of ripple is evident across the scene. This ripple is consistent with the uniform scene reconstructions presented by *Tanner* [1990]. The ripple is unavoidable with the current ESTAR reconstruction algorithm because the subspace spanned by the interference patterns does not include a uniform brightness temperature distribution.

The ripple in the uniform scene reconstruction can be reduced by transforming the subspace of possible images. To the extent that a common antenna element pattern $P(\phi)$ does exist for all interference patterns, a uniform scene is essentially a measurement of $P(\phi)$. Thus for uniform or near uniform scenes a transformation based on the shape of the zeroth visibility "interference" pattern is appropriate since it approximates the antenna element pattern. Normalization of the interference patterns by $P(\phi)$ should place the uniform scene in (or near) the subspace of reconstructable images. This normalization is given by

$$\tilde{V}_n(\phi) = \frac{V_n(\phi)}{V_0(\phi)} \tag{13}$$

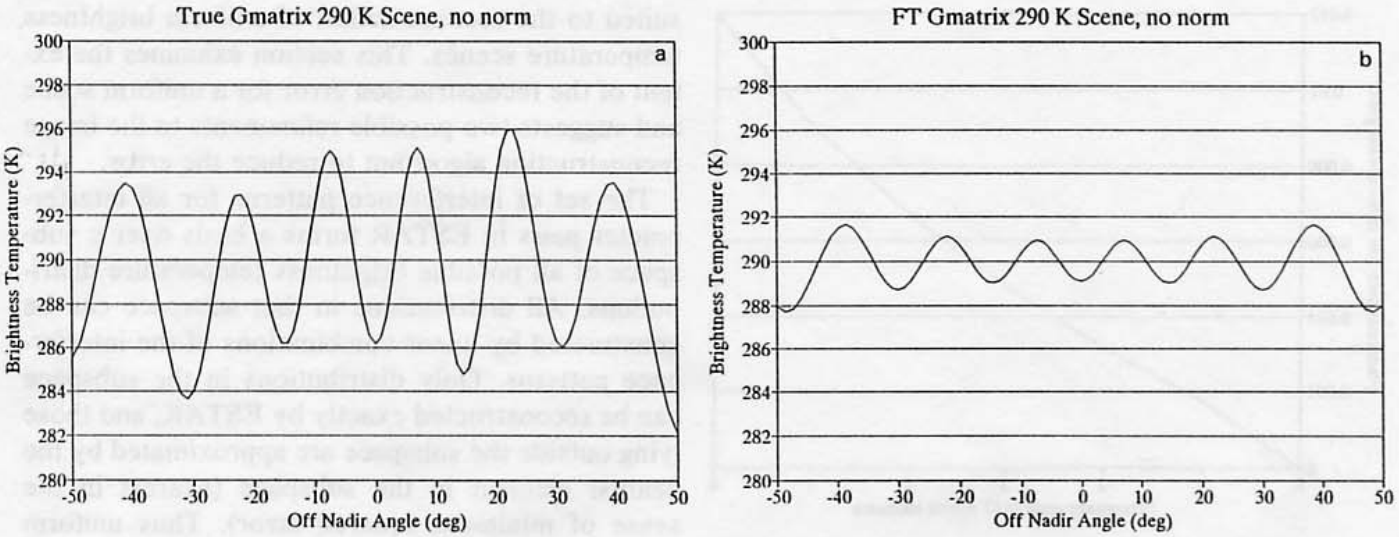

Fig. 8. Theoretical image reconstruction of a uniform 290 K scene using the present ESTAR algorithm. The ripple in the images are caused by the truncation of the sampled visibility function at lower spatial harmonics due to the antenna element pattern. (*a*) Using the measured ESTAR interference patterns, the rms error in the image is 3.5 K. (*b*) Using the ideal Fourier transform interference patterns, the rms error in the image is 1.0 K.

where $\bar{V}_n$ is the normalized interference pattern for the nth visibility sample and $V_0(\phi)$, the zeroth interference pattern, is the approximate element pattern $P(\phi)$. The image reconstruction algorithm would then be modified to remap, or unnormalize, the image back to the original brightness temperature subspace by

$$\hat{T}_B(\phi) = \frac{1}{V_0(\phi)} [\bar{G}^{\dagger}(\bar{G}\bar{G}^{\dagger})^{-1}\, \mathbf{V}] \tag{14}$$

where $\bar{G}$ is the normalized $\bar{G}$ matrix with interference patterns given by (13). This reconstruction algorithm is demonstrated in Figure 9 for both the measured and the ideal interference patterns. In both cases the ripple has been reduced relative to the unnormalized reconstruction shown in Figure 8. For the measured interference patterns the rms error in the image has been reduced from 3.5 to 2.4 K, and for the ideal interference patterns from 1.0 to 0.3 K. The greater improvement in the case of the ideal pattern is due to the unique antenna element patterns which was assumed. A consistent cosine envelope, shown in Figure 3*b*, was used for all interferometer pairs, and the normalization given by (13) was more meaningful. This improvement highlights the importance of reducing the variations in the interference pattern envelope between interferometer pairs in the ESTAR instrument. This can be done, for example, by reducing the mechanical support structure extending out beyond the ground plane of the antenna array (C. T. Swift and A. Griffis, personal communication, 1991).

The ripple present in the image of uniform scenes is a consistent feature of the reconstruction algorithm. As such, it can be accounted for when interpreting ESTAR images. For example, the image reconstructed from the following brightness temperature distribution

$$T_B(\phi) = 291 \text{ K} \qquad |\phi| < \text{HPBW} \tag{15a}$$

$$T_B(\phi) = 290 \text{ K} \qquad \text{otherwise} \tag{15b}$$

will largely reproduce the ripples in the image of the uniform scene. The difference between the image of (15) and that of the uniform scene is shown in Figure 10. The large ripples due to the 290 K offset have been removed and the remaining ripples, due only to the 1 K perturbation, have been scaled down proportionately. This correction follows naturally from the linearity of the image reconstruction algorithm. In practice, this approach can be utilized when interpreting ESTAR images. Perturbation images, representing the change in brightness temperature relative to a nominal distribution, would scale the inherent ripples in the reconstructed image down by the relative size of the perturbation. For

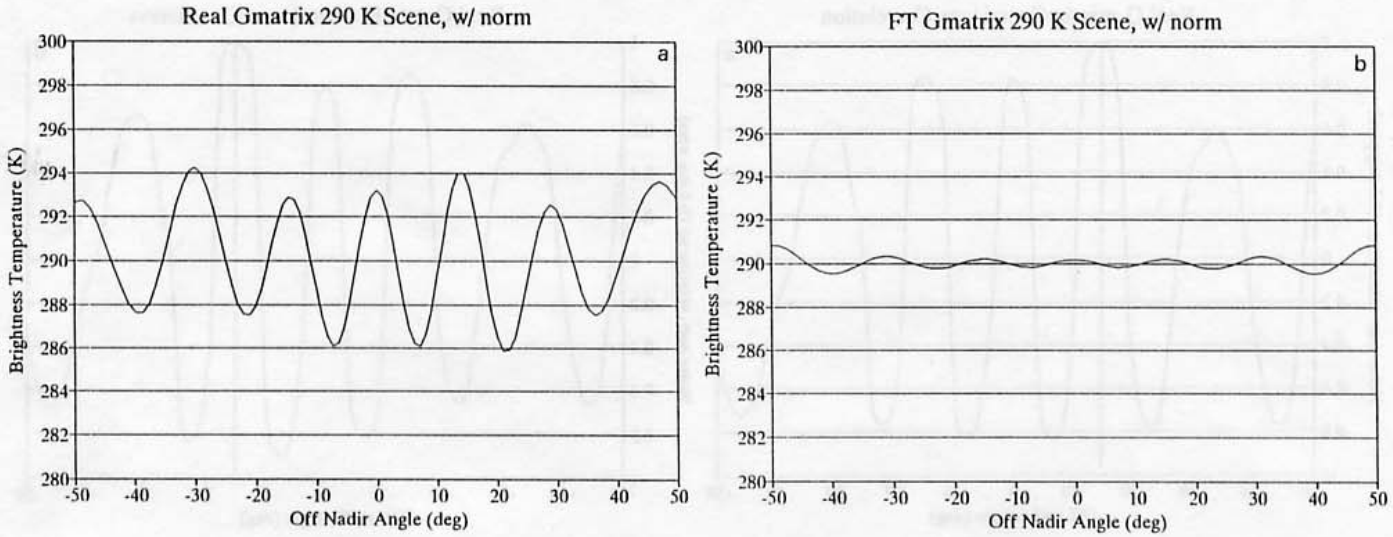

Fig. 9. Theoretical image reconstruction of a uniform 290 K scene using a modified algorithm which normalizes all interference patterns by the zeroth "interference" pattern. This places the uniform brightness temperature distribution closer to the subspace spanned by the set of interference patterns. (*a*) Using the measured ESTAR interference patterns, the rms error in the image is 2.4 K. (*b*) Using the ideal Fourier transform interference patterns, the rms error in the image is 0.3 K.

example, open ocean ESTAR images could retrieve salinity perturbations about a mean cross track salinity distribution. The expected range of salinity induced changes in the brightness temperature at 1.4 GHz, 5–10 K at 0° incidence angle [*Klein and Swift*, 1977], compares with a 100 K brightness temperature offset. This represents a factor of 10–20 potential reduction in image ripple.

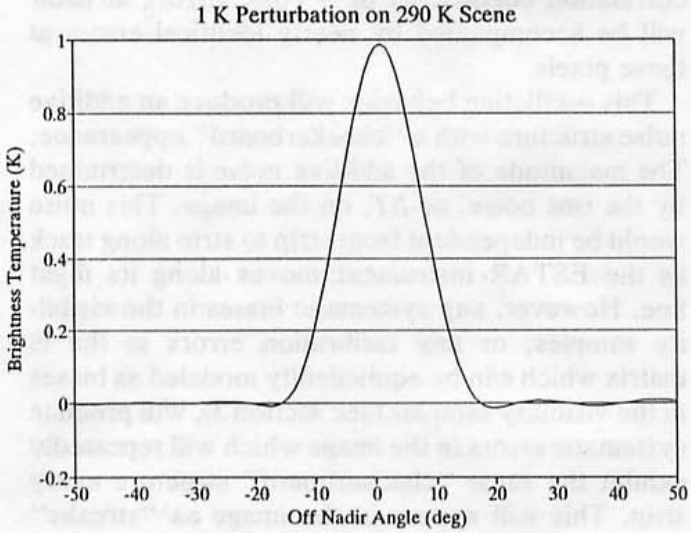

Fig. 10. The difference between a 290 K image and the same image with a 1 K increase at the center pixel. By linearity this is equivalent to an image of just the 1 K pixel. Note that the ripples in the image have been scaled down, relative to those in the 290 K uniform image, by the relative brightness temperature. Perturbation image interpretation would produce a similar scaling down of the ripple artifact.

5. IMAGE COVARIANCE STRUCTURE

The covariance Γ_T on the reconstructed image $\hat{\mathbf{T}}$, is given by (11). In order to evaluate this expression, the form of the covariance on the visibility measurements Γ_v must be known. The correlation between different samples of the visibility function is evaluated explicitly in the appendix. For reasonable predetection RF bandwidths B and postdetection integration times τ, the condition $B \gg 1/\tau$ forces the noise in the different visibility samples to be essentially uncorrelated. This results in a diagonal visibility covariance matrix.

The image covariance matrix Γ_T (and covariance matrices in general) can be factored into the following form

$$\Gamma_T = \mathsf{SRS} \tag{16}$$

where S is a diagonal matrix of standard deviations and R is a symmetric matrix of correlation coefficients. Elements of R, r_{ij}, represent the degree of correlation between the noise in the ith and jth pixels in the brightness temperature image. Diago-

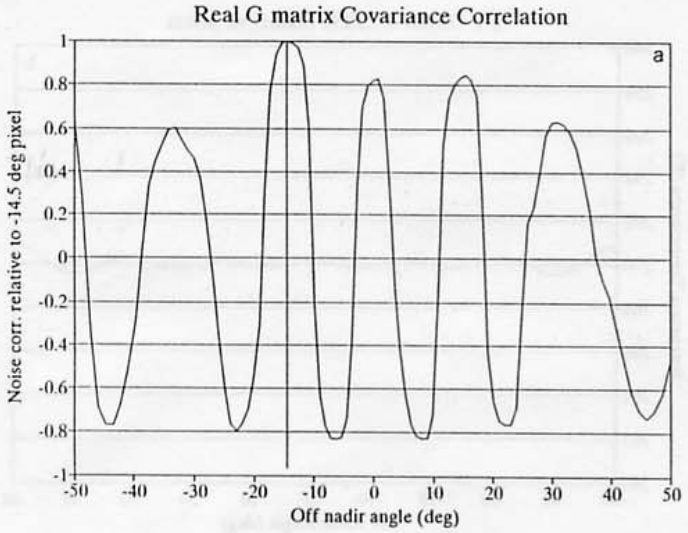

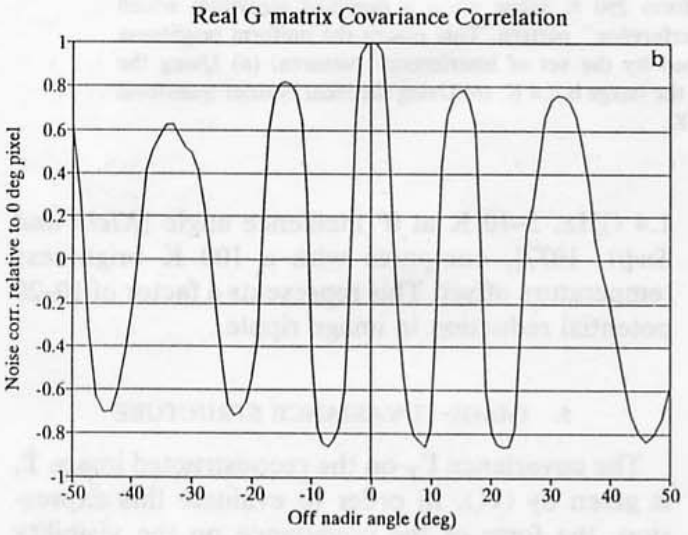

Fig. 11. Correlation of the error (due to both noise and systematic offsets) in one pixel of the ESTAR image with the error in other pixels. The large negative and positive correlation is due to the cross coupling of spatial harmonics between the different visibility samples. The frequency of oscillation of the correlation is determined by the spatial resolution of the image. (*a*) Correlation relative to the image pixel at −14.5° cross track; (*b*) correlation relative to the nadir pixel; (*c*) correlation relative to the +15.4° pixel.

nal elements of R, r_{ii}, are by definition all equal to unity. Several of the rows of the correlation matrix R are shown in Figure 11. Included are the rows corresponding to pixels located at off-nadir angles of −15°, 0°, and +15°. The correlation function is seen to oscillate between very strong positive and negative correlations at a periodicity corresponding to the spatial resolution of the image. For example, the correlation function for the 0° (nadir) pixel is

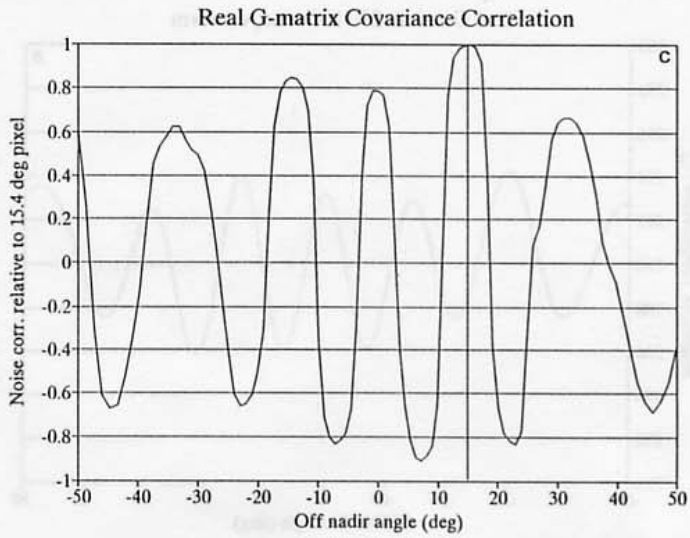

Fig. 11. (continued)

unity at 0°, then decreases to ≈−0.85 at the first two independent pixels on either side. This implies that noise (or systematic offsets) in the brightness temperature image at nadir due to noise (or systematic offsets) in the visibility function will be strongly negatively correlated with the noise (or systematic offsets) in the image at ≈±7°. Positive errors at nadir will be accompanied by negative errors of nearly the same magnitude at ±7°. The next independent pixels out from nadir, at ≈±15°, have correlation coefficients of ≈+0.8. Errors at nadir will be accompanied by nearly identical errors at these pixels.

This oscillating behavior will produce an additive noise structure with a "checkerboard" appearance. The magnitude of the additive noise is determined by the rms noise, or ΔT, on the image. This noise would be independent from strip to strip along track as the ESTAR instrument moves along its flight line. However, any systematic biases in the visibility samples, or any calibration errors in the G matrix which can be equivalently modeled as biases in the visibility samples (see section 3), will produce systematic errors in the image which will repeatedly exhibit the same "checkerboard" structure every strip. This will appear in the image as "streaks" running parallel to the flight line and oscillating at a periodicity corresponding to the spatial resolution of the image. The magnitude of these streaks depends on the size of the systematic errors in G or V. Systematic errors in the absolute calibration of conventional microwave radiometers are quite of-

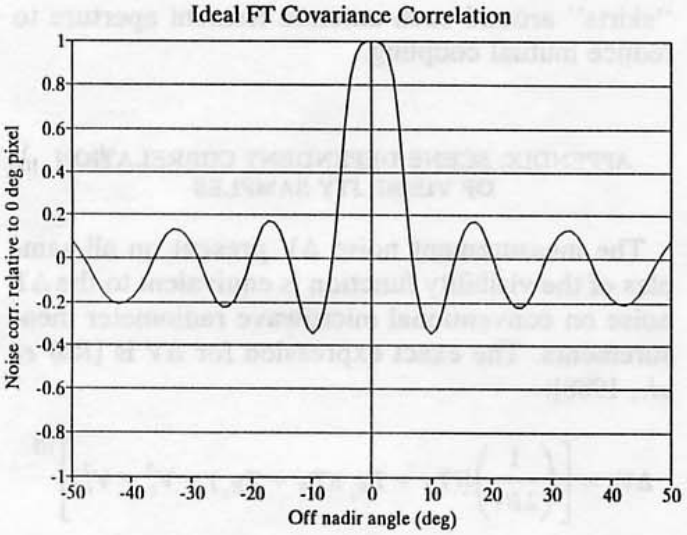

Fig. 12. Correlation of the error in the nadir pixel with the error in other pixels for the ideal Fourier transform visibility samples. The correlation damps out with a sin x/x behavior because the noise on the visibility measurements determines the power spectrum of the noise on the image.

ten several orders of magnitude greater than the precision, or ΔT, of the instruments, and the same should be expected for ESTAR. Correcting for this correlation structure would involve first identifying its magnitude through a correlation analysis of a large set of ESTAR flight images, then simply treating it as a known systematic bias and subtracting it.

The cause of the large correlation between errors at widely separated angles in the image, as well as a possible approach to reducing it, is apparent by considering the covariance structure of the brightness temperature image reconstructed from the ideal Fourier transform interference patterns. The row of the correlation matrix factored from this covariance matrix which corresponds to the nadir pixel is shown in Figure 12. This image covariance also assumes an uncorrelated, diagonal, visibility covariance. In the case of true Fourier transform relationships between visibility and image vectors the interpretation is straightforward. The assumption of a diagonal visibility covariance is equivalent to assuming independent white noise in the visibility Fourier domain. The noise is "band limited" in this case by the maximum interferometer pair spacing of the visibility samples. Thus the power spectral density of the noise in the image can be described by

$$S_{\Delta T}(d) = \Delta V^2 \qquad |d| \le 3.5\lambda \tag{17a}$$

$$S_{\Delta T}(d) = 0 \qquad \text{otherwise} \tag{17b}$$

where ΔT is the rms noise on the image, d is the separation between interferometer pairs, and ΔV is the rms noise on the visibility samples. The autocorrelation of the image noise follows as the Fourier transform of $S_{\Delta T}(d)$, by the Wiener-Khinchin theorem [*Papoulis*, 1984]:

$$\langle \Delta T(\sin\phi)\, \Delta T(\sin\phi - \sin\phi') \rangle = \Delta V^2 \frac{2d_{\max}}{\lambda} \operatorname{sinc}\left(\frac{2d_{\max}}{\lambda} \sin\phi'\right) \tag{18}$$

where $\Delta T(\sin\phi)$ is the rms noise on the image at sin ϕ, the expectation operation $\langle \cdot \rangle$ is over the complete image with respect to sin ϕ, $d_{\max} = 3.5\lambda$ is the maximum interferometer pair spacing, and sinc $(x) = \sin(\pi x)/\pi x$. The correlation structure in Figure 12 clearly reflects a sinc (x) behavior. The periodicity of the correlation, sin $\phi = \lambda/d_{\max}$, is determined by the resolution HPBW $= d_{\max}/\lambda$. Images generated from true Fourier transform visibility samples will be largely free from systematic along track streaking and cross track "checkerboard" artifacts.

The measured G matrix covariance structure exhibits a weakly decaying correlation in both directions away from unity correlation at the pixel lying on the main diagonal of Γ_T. This is a result of the dominant spatial harmonic present in each visibility sample. However, the large degree of cross coupling of harmonics between the different visibility samples has introduced a significant degree of "color" into the power spectral density of the noise in the reconstructed image. This, in turn, degrades the ideal sinc (x) correlation structure. Aside from calibrating out the systematic streaks introduced by the structure of the image covariance, a more direct solution might be to reduce the degree of harmonic coupling in the visibility samples. The predominant source of this coupling was identified in section 3, above, as multipath induced secondary interferometer pairs. Possible hardware modifications to reduce the multipath include recessing the antenna support structure surrounding the array ground plane, as discussed in section 4, and electrically decoupling adjacent and other nearby array elements, for example, by adding corrugated, flared

"skirts" around the perimeter of the aperture of each antenna element.

6. CONCLUSIONS

The image reconstruction algorithm presently used by the ESTAR aircraft instrument introduces "streaking" artifacts into the image for a variety of different reasons. Truncation of the lower visibility spectrum due to the antenna element pattern envelope on the zeroth visibility "interference" pattern introduces a significant ripple in the reconstruction of images with relatively little brightness temperature contrast. This reconstruction error has an rms value of 3.5 K across a $T_B = 290$ K uniform scene. The cross track ripple will appear as streaks in the image oriented along the instrument flight line. The error can be reduced to an rms value of 2.4 K by a transformation of the subspace of brightness temperature distributions spanned by the interference patterns of the visibility samples. This transformation consists of an element-pattern-based renormalization of the interference patterns. Limitations with this approach are due to small inconsistencies between the different antenna element patterns. An ideal antenna array, with identical element patterns, is shown to suffer a 1.0 K rms reconstruction error without element pattern renormalization. This error is reduced to 0.3 K with the transformation. Future improvements in the ESTAR antenna hardware should result in an rms reconstruction error between 2.4 and 0.3 K.

Multipath scattering of the incoming signal produces interference patterns with a strong primary harmonic component and a significant secondary distribution of effective interferometer pair spacings. A spectral analysis procedure is presented which identifies and quantifies the secondary harmonic contributions in terms of the antenna hardware design. The coupling of spatial harmonics between the visibility samples introduces a very strong correlation between the noise in the image at widely separated pixels. This correlation will also appear as streaks running parallel to the flight line of the ESTAR aircraft. The correlation can in principle be detected by a covariance analysis of the image and then corrected. However, the source of the cross coupling between spatial harmonics can also be reduced by careful antenna design. Possible design improvements include a lower electrical profile for the array backup structure and corrugated "skirts" around each antenna element aperture to reduce mutual coupling.

APPENDIX: SCENE DEPENDENT CORRELATION OF VISIBILITY SAMPLES

The measurement noise ΔV present on all samples of the visibility function is equivalent to the ΔT noise on conventional microwave radiometer measurements. The exact expression for ΔV is [*Ruf et al.*, 1988]:

$$\Delta V_r = \left[\left(\frac{1}{2B\tau}\right)[(T_B + T_{R_1})(T_B + T_{R_2}) + V_r^2 - V_i^2]\right]^{1/2} \tag{A1}$$

$$\Delta V_i = \left[\left(\frac{1}{2B\tau}\right)[(T_B + T_{R_1})(T_B + T_{R_2}) + V_i^2 - V_r^2]\right]^{1/2} \tag{A2}$$

where V_r and V_i are the real and imaginary components of V, B is the predetection bandwidth of the measurements, τ is the postdetection integration time, T_B is the average brightness temperature over the antenna element pattern, and T_{R_1} and T_{R_2} are the receiver noise temperatures of the two channels of the interferometer pair. This appendix examines the degree of correlation between the noise in two different samples of the visibility function. Clearly, noise originating from the receivers, T_R, will be independent, provided the two interferometer pairs share no common hardware. However, that portion of ΔV due to the scene brightness temperature may be correlated.

Following the noise process formalism developed by *Ruf et al.* [1988], a complex visibility sample can be expressed as

$$V_n(t) = \frac{1}{\tau}\int_{t-\tau/2}^{t+\tau/2} b_i(t')b_j^*(t')\,dt' \tag{A3}$$

where $V_n(t)$ is the noisy nth visibility sample, with standard deviation given by (A1) and (A2) and with mean given by (1). V_n results from the low-pass filtering of the cross correlation of interferometer channels i and j. The noise processes b_{ij} at the two antennas are defined by

$$b_i(t) = \int_0^{2\pi} \int_0^{\pi} b(\theta, \phi; t)\, e^{jkr_i(\theta,\phi)} \sin\theta\, d\theta\, d\phi \qquad \text{(A4)}$$

where $b(\theta, \phi; t)$ is a stochastic thermal noise process with power spectral density given by

$$S_b(f) = T_B(\theta, \phi)/2B \qquad |f| \text{ in the RF passband} \qquad \text{(A5}a\text{)}$$

$$S_b(f) = 0 \qquad \text{otherwise} \qquad \text{(A5}b\text{)}$$

and where $k = 2\pi/\lambda$, with λ the RF wavelength, and $r_i(\theta, \phi)$ is the distance from the thermal emission source at (θ, ϕ) to the ith antenna element.

The correlation between two visibility samples, $V_n(t)$ and $V_m(t)$, is found by examining the expectation of their product

$$\langle V_n(t)V_m^*(t)\rangle = \left\langle \frac{1}{\tau}\int_{t-\tau/2}^{t+\tau/2} b_i(t')b_j^*(t')\, dt' \cdot \frac{1}{\tau}\int_{t-\tau/2}^{t+\tau/2} b_k^*(t'')b_1(t'')\, dt'' \right\rangle \qquad \text{(A6)}$$

where the nth visibility sample corresponds to the cross correlation of the ith and jth channels and the mth sample to the kth and lth channels. Exchanging the order of expectation and integration operations gives

$$\langle V_n(t)V_m^*(t)\rangle = \frac{1}{\tau^2}\int_{t-\tau/2}^{t+\tau/2}\int \langle b_i(t')b_j^*(t')b_k^*(t'')b_1(t'')\rangle\, dt'\, dt'' \qquad \text{(A7)}$$

the expectation operation can be expanded using the identity [*Evans and McLeish*, 1977]:

$$\langle abcd\rangle = \langle ab\rangle\langle cd\rangle + \langle ac\rangle\langle bd\rangle + \langle ad\rangle\langle bc\rangle \qquad \text{(A8)}$$

and solving for the autocorrelation, $R_{b_i}(\tau)$, of $b_i(t)$ from (A5),

$$R_{b_i}(\tau) = \langle b_i(t)b_i^*(t-\tau)\rangle \qquad \text{(A9}a\text{)}$$

$$R_{b_i}(\tau) = T_B(\theta, \phi)\ \text{sinc}\ (B\tau)\cos(2\pi f_c\tau) \qquad \text{(A9}b\text{)}$$

where $\text{sinc}\ (x) = \sin(\pi x)/\pi x$ and $f_c = c/\lambda$ is the RF center frequency. Combining (A7), (A8), and (A9) gives

$$\langle V_n(t)V_m^*(t)\rangle = \frac{1}{\tau^2}\int_{t-\tau/2}^{t+\tau/2}\int \{\langle V_n\rangle \cdot \langle V_m^*\rangle\ \text{sinc}^2\,[B(t'-t')]\cos^2[2\pi f_c(t'-t')] + \langle V_{ik}\rangle\langle V_{jl}^*\rangle\ \text{sinc}^2\,[B(t'-t'')]\cos^2[2\pi f_c(t'-t'')] + \langle V_{il}\rangle\langle V_{jk}^*\rangle\ \text{sinc}^2\,[B(t'-t'')]\cos^2[2\pi f_c(t'-t'')]\}\, dt'\, dt'' \qquad \text{(A10)}$$

where the terms V_{ab} represent the visibility samples measured by cross correlating the ath and bth channels. The first term inside the integral in (A10) is independent of t' and t'' and can be factored through the integral. The second and third terms, which include the factor $\text{sinc}^2\,[B(t'-t'')]\cos^2[2\pi f_c(t'-t'')]$, will integrate to zero for $B \gg 1/\tau$ and $f_c \gg 1/\tau$. This leaves

$$\langle V_n(t)V_m^*(t)\rangle = \langle V_n\rangle\langle V_m^*\rangle \qquad \text{(A11)}$$

This demonstrates that separate samples of the visibility function have uncorrelated ΔV noise components. The result is necessary in order to assume a diagonal structure for the covariance Γ_V on V.

Acknowledgments. The author would like to express his gratitude to C. T. Swift and A. Griffis of the University of Massachusetts and to D. M. Le Vine of NASA Goddard Space Flight Center for supplying all the ESTAR data needed for this analysis. Also acknowledged are helpful discussions concerning the ESTAR image reconstruction algorithm with A. B. Tanner and valuable comments and suggestions made by U. R. Kraft, A. S. Milman, and N. Skou. This work was carried out at the Jet Propulsion Laboratory, California Institute of Technology, Pasadena, under contract to the National Aeronautics and Space Administration.

REFERENCES

Evans, G., and C. W. McLeish, *RF Radiometer Handbook*, Artech House, Dedham, Mass., 1977.

Hiett, T. C., Construction of an electronically steered thinned array radiometer, M.S. thesis, Dep. of Electr. and Comp. Eng., Univ. of Mass., Amherst, Sept. 1988.

Klein, L. A., and C. T. Swift, An improved model for the dielectric constant of sea water at microwave frequencies, *IEEE Trans. Antennas Propag.*, *AP-25*, 104–111, 1977.

Leech, J., On the representation of $1, 2, \cdots, n$ by differences, *J. London Math. Soc.*, *31*, 160–169, 1956.

Le Vine, D. M., M. Kao, A. B. Tanner, C. T. Swift, and A. Griffis, Initial results in the development of a synthetic aperture microwave radiometer, *IEEE Trans. Geosci. Remote Sens.*, *28*(4), 614–619, 1990.

Moffett, A. T., Minimum redundancy linear arrays, *IEEE Trans. Antennas Propag.*, *16*, 172–175, 1968.

Murphy, R., et al., High resolution multifrequency microwave radiometer instrument panel report, vol. IIe, Earth Observ. Sys., Natl. Aeronaut and Space Admin., Washington, D. C., 1987.

Papoulis, A., *Probability, Random Variables, and Stochastic Processes*, McGraw-Hill, New York; 1984.

Ruf, C. S., Antenna performance for a synthetic aperture microwave radiometer in geosynchronous Earth orbit, in *Proceedings of the 1990 International Geoscience and Remote Sensing Symposium*, vol. II, pp. 1589–1592, Institute of Electrical and Electronics Engineers, New York, May 1990.

Ruf, C. S., C. T. Swift, A. B. Tanner, and D. M. Le Vine, Interferometric synthetic aperture microwave radiometry for the remote sensing of the Earth, *IEEE Trans. Geosci. Remote Sens.*, *26*(5), 597–611, Sept. 1988.

Tanner, A. B., Aperture synthesis for passive microwave remote sensing: The electronically steered thinned array radiometer, Ph.D. dissertation, 173 pp., Dep. of Electr. and Comp. Eng., Univ. of Mass., Amherst, Feb. 1990.

C. S. Ruf, M/S 168-327, Jet Propulsion Laboratory, California Institute of Technology, 4800 Oak Grove Drive, Pasadena, CA 91109.